Science Advances

Supplementary Materials for

Electrical 180° switching of Néel vector in spin-splitting antiferromagnet

Lei Han *et al.*

Corresponding author: Cheng Song, songcheng@mail.tsinghua.edu.cn; Junwei Liu, liuj@ust.hk;
Feng Pan, panf@mail.tsinghua.edu.cn

The PDF file includes:

Texts S1 to S7
Figs. S1 to S20
Legend for movie S1
References

Other Supplementary Material for this manuscript includes the following:

Movie S1

Supplementary Text

Text S1: Basic characterizations and transport measurements of Mn_5Si_3 thin films

As shown in fig. S2A, XRD spectrum of Mn_5Si_3(80 nm) film shows a strong Mn_5Si_3(0001) texture with average roughness R_a of 1.27 nm (fig. S2C). The phase transition property of Mn_5Si_3 thin films can be cross-checked by multiple characterizations. First, temperature-dependent longitudinal resistivity ρ_{xx} (fig. S2D) and its temperature-derivative curve (fig. S2E) reveal two minimum points at 230 K and 60 K, corresponding to T_{N2} of paramagnetic-to-cAFM and T_{N1} of cAFM-to-ncAFM magnetic phase transitions, respectively, consistent with reported measurements on Mn_5Si_3 thin films ([29]). Second, we carried out in-situ XRD measurements of Mn_5Si_3(0002) peak from 20 K to 300 K (fig. S2B), where temperature-dependent lattice parameter c was extracted and shown in fig. S2F. c abruptly decreases when increasing temperature across T_{N1}, which is due to the structural transition accompanied with the ncAFM-to-cAFM magnetic phase transition. In contrast, c linearly increases without abrupt change when increasing temperature across T_{N2}, which proves that the hexagonal crystal structure with broken $t\mathcal{T}$ symmetry is preserved from PM to cAFM, bringing about perquisites for the spin-splitting band structure and AHE in the cAFM phase. These results on structural transition match with former results on Mn_5Si_3 thin films ([29]). Third, we carried out temperature-dependent time-resolved reflectivity measurements on Mn_5Si_3 thin film between 200 K and 270 K with a step of 5 K to further verify the absence of structural transition at T_{N2}. As shown in the 2D plot of fig. S2H (where a typical curve at 220 K is presented at fig. S2G with metallic excitation-relaxation behavior), no obvious signature of structural transition within this temperature range can be observed.

Figure S3 shows the hysteresis of Hall resistivity and magnetization of Mn_5Si_3(80 nm) with corresponding field-derivative curves measured under different temperatures. It can be seen that there are two abrupt changes around zero field and at higher fields in magnetization hysteresis (fig. S3B), as verified by corresponding peaks in field-derivative curves (fig. S3D). Notably, the peaks at higher fields in field-derivative curves of magnetization have the same locations with those in field-derivative curves of Hall resistivity, consistent with Fig. 2A and Fig. 2B. No notable AHE or AHE-related net moment m is observed at 240 K, which is because of the transition from cAFM to PM above 230 K as confirmed in fig. S2.

<u>Text S2: Further discussions on the origin of AHE</u>
First, clearly, the net moment with coercive field of around zero (denoted by the black line in Fig. 2B) does not contribute to ρ_{yx}, because there is no abrupt change in ρ_{yx} near zero field. Moreover, the magnitude of this net moment is closely related to crystallinity. As shown in fig. S5, this net moment can be drastically suppressed in fig. S5E as compared with fig. S5B, when the peak intensity of Mn_5Si_3(0002) is enhanced by an order of magnitude in fig. S5D as compared with fig. S5A. This is achieved by using another sputtering process, where Mn_5Si_3 is directly deposited on Al_2O_3 substrate at 600 °C, instead of first depositing at 465 °C followed by annealing at 600 °C. Nevertheless, the roughness of film by directly depositing at 600 °C increases drastically in fig. S5F as compared with fig. S5C, which is why we did not adopt this sputtering process.

Second, the net moment m with relatively large coercive field (denoted by the blue line in Fig. 2B) cannot explain the observed AHE. The Hall resistivity ρ_{yx} for cAFM Mn_5Si_3 at 150 K is 0.1~0.2 microhm cm (fig. S6), which is comparable to that of typical ferromagnets (*49, 50*). However, m for Mn_5Si_3 ranges in 1~10 emu cm^{-3} as measured by SQUID (fig. S6), which is several orders of magnitudes smaller than that for typical ferromagnets (*49, 50*). 1~10 emu cm^{-3} can be transformed into 2.5~25 milli μ_B per magnetic Mn atom, equaling only 1~10 ‰ of Mn atomic spin of 2.4 μ_B. More importantly, fig. S6 shows that m varies for samples of different thicknesses, but ρ_{yx} almost remains unchanged, further ruling out the possibility that ρ_{yx} comes from m (*49, 50*). Note that m is relatively larger for thinner Mn_5Si_3 film with stronger interfacial inversion symmetry breaking, which is consistent with the physical picture that the magnitude of DMI is positively correlated with the degree of symmetry breaking (*48*).

The discussions above reveal that the measured AHE cannot be attributed to net moment. Moreover, inline image of fig. S3A shows opposite temperature dependence of ρ_{yx} and ρ_{xx}, excluding extrinsic mechanisms of AHE which should show a positive correlation between ρ_{yx} and ρ_{xx} (*49, 50*). We further carried out Hall resistivity measurements on Mn_5Si_3 film with different width of Hall bar, as shown in fig. S7. For typical ferromagnets, the coercive field of AHE hysteresis should exhibit a trend of first increasing and then decreasing as the width of Hall bar decreases (*67, 68*). This phenomenon can be well-explained by combining both the single domain and the multi domain switching mechanism. When the width of Hall bar is much larger than the nucleation diameter D_n, the multidomain switching mechanism takes place, where the coercive field is determined by reversal domain nucleation and domain wall motion (*69, 70*). Thus, the decrease of channel width means more limitations on reversal domain nucleation sites (*69*) and enhanced domain wall pinning by edge defects (*70*), leading to the increase of coercive field. When the width of Hall bar is smaller than D_n, the single-domain switching mechanism dominates, where the coercive field is dependent on the thermal stability factor $\varDelta$ and corresponding Arrhenius thermal activation model (*68*). Hence, the coercive field decreases with the decrease of channel width due to reduced $\varDelta$. Worth noting that, D_n as a critical parameter is quite small (tens of nanometers) for ferromagnets (*68*). In contrast, the coercive field of our cAFM Mn_5Si_3 starts to decrease when channel width is below 500 nm (fig. S7), revealing a much larger D_n on the order of hundreds of nanometers. This indicates the AFM domain with larger size and is consistent with measurements on AFM Mn_3Sn (*71, 72*). As a result, the experimentally observed AHE should be attributed to the intrinsic Néel vector-dependent Berry curvature.

Text S3: Discussions on critical parameters for simulations and calculations

Exchange interaction constant. Four nearest exchange coupling J_1, J_2, J_3, and J_4 were considered for simulations and calculations, where J_1 and J_2 are AFM coupling while J_3 and J_4 are FM coupling (fig. S8). Note that in some previous theoretical works, J_4 as AFM coupling is energetically favorable for bulk crystal Mn_5Si_3 (64, 65). This leads to a $t\mathcal{T}$ symmetry to connect antiferromagnetic sublattice, which will quench the AHE (fig. S9A). However, we have experimentally observed AHE in the cAFM phase of Mn_5Si_3 thin films, which means that the most possible scenario is J_4 becomes FM coupling in our Mn_5Si_3 thin films without $t\mathcal{T}$ symmetry (fig. S9B), consistent with former measurements on Mn_5Si_3 thin films (29).

Magnetic easy axis. The magnetic easy axis in our cAFM-phase Mn_5Si_3 thin film is set along (1,1,1) direction in the Cartesian coordinate system xyz for simulations and calculations (Refer to Fig. 1A for the definition of Cartesian coordinate system xyz), matching previous experimental works (29). Note that for some theoretical works (64, 65), the easy axis of cAFM phase Mn_5Si_3 is along crystalline b axis of its orthogonal cell, which is the y axis in our Cartesian coordinate system. Nevertheless, Néel vector completely along y axis does not allow the emergence of σ_{xy} (Fig. 2G), which contradicts with our experimental measurements. Indeed, Néel vector tilting from in-plane direction is required to generate our experimentally observed σ_{xy}, which is reasonable for thin films with epitaxial strain (26). We set the easy axis along (1,1,1) as a direction tilting from y for simplicity without loss of genericity, supported by DFT calculated magnetocrystalline anisotropy energy (MAE) for different in-plane and out-of-plane orientations of Néel vector (fig. S9C). It turns out that the MAE is quite small, on the order of ± 0.4 meV per unit cell compared with Néel vector along (1,1,1), corresponding to 0.1 meV per magnetic Mn atom. Hence, the magnitude of uniaxial anisotropy constant K for simulation is set to be 0.1 meV, matching the DFT-obtained value. Note that it is the electrical 180° switching of the Néel vector that we aim to demonstrate, where the precise direction of Néel vector or its tilting angle to the in-plane direction does not influence the main idea of this work. In fact, the general 180° switching mechanism that we proposed only forbids the Néel vector n in the plane of net moment m and spin polarization p, but does not require the Néel vector to be along some certain directions (Supplementary text S4). To figure out the direction of Néel vector in cAFM Mn_5Si_3, neutron scattering is needed, which is quite difficult for our thin films with relatively lower crystal quality than single crystal.

DMI vector. We performed DFT calculations to give an estimation of the DMI vector d, resulting in DMI energy of around 1 meV, which is an order of magnitude larger than MAE. We start from the classical spin model, with the Hamiltonian for each unit cell written as:

$$H = \sum_{<p,q>} J_{p,q} m_p \cdot m_q + \sum_{<p,q>} d_{p,q} \cdot (m_p \times m_q) - K \sum_p (k \cdot m_p)^2$$

Where $J_{p,q}$ and $d_{p,q}$ refer to the exchange interaction constant and the DMI vector between magnetic Mn atom p and q (p, q = 1, 2, 3, 4), respectively. K is the uniaxial anisotropy constant. m_p (m_q) denotes the magnetic moment of Mn_p (Mn_q) atom and k is the direction of easy axis. As shown in fig. S9D, considering two adjacent magnetic Mn atoms (Mn_1 and Mn_2) as an example, there are two mirror planes passing through and perpendicular to the line connecting Mn_1 and Mn_2 for ideal single crystal, denoted as M_{xy} and M_{xz}. Thus, based on symmetry analysis, only DMI vector along z direction (d_{12}^z) is permitted (73). We first focus on d_{12}^z between Mn_1 and Mn_2, where four spin configurations are considered (fig. S9E–H) with spin orientations of Mn_1 and Mn_2 along x and y,

respectively: (i). $m_1 = (S, 0, 0)$, $m_2 = (0, S, 0)$, (ii). $m_1 = (-S, 0, 0)$, $m_2 = (0, S, 0)$, (iii). $m_1 = (S, 0, 0)$, $m_2 = (0, -S, 0)$, (iv). $m_1 = (-S, 0, 0)$, $m_2 = (0, -S, 0)$. Therefore, we can express the energy of our spin model as:

$$E = d_{12}^z m_1^x m_2^y - m_1^x \sum_{p \neq 1} d_{1p}^y m_p^z + m_2^y \sum_{p \neq 2} d_{2p}^x m_p^z + E_{otherterm}$$

Now we can examine the energies for these four spin configurations, i.e., E_i, E_{ii}, E_{iii}, E_{iv} from SCF calculations by VASP, which gives d_{12}^z equaling $\frac{1}{4S^2}(E_i + E_{iv} - E_{ii} - E_{iii})$ of 1.16 meV. For our epitaxial Mn_5Si_3 film on the Al_2O_3 substrate, M_{xy} is naturally broken, which means that d_{12}^x is actually permitted. We can model this symmetry breaking by a little displacement of one layer of magnetic Mn atoms and follow similar method for estimating d_{12}^z, which gives d_{12}^x of around 1 meV. Different little displacements have been tested, which all lead to consistent estimation of d_{12}^x with the magnitude of around 1 meV. Similar results were obtained through TB2J package (74, 75) based on Green's function method, which generates DMI magnitude of 0.93 meV. For atomic spin simulations, only d_{12}^x is considered for simplicity, because d_{12}^z cannot bring about the SQUID-obtained out-of-plane net moment m_z. d_{12}^x is set to be 1.35 meV for simulation, which gives a simulated m_z of 5‰, consistent with SQUID results (Supplementary text S2) and matching the DFT estimated d_{12}^x. We also performed control simulations considering finite d_{12}^x and d_{12}^z, which show no essential difference.

Critical switching damping-like effective field. H_{DL}, as the magnitude of the damping-like effective field $H_{DL,ia}$ introduced in Materials and Methods, can be link to the damping-like SOT magnitude ξ_{DL} and the current density J by the following equation (26):

$$\xi_{DL} = \frac{\hbar|\gamma|J\theta}{2em_st} = |\gamma|H_{DL} = |\gamma|\frac{\hbar J\theta}{2em_st}$$

Where $\hbar$, γ, θ, e, m_s, and t are the reduced Planck's constant, the gyromagnetic ratio of the electron, the spin Hall angle of Pt, the electron charge, the saturation magnetization of magnetic Mn atom for Mn_5Si_3, and the thickness of Mn_5Si_3, respectively. The critical H_{DL} is 8.66 kOe from atomic spin simulations, which results in a simulated critical switching current density J_c of 3149 MA cm^{-2}, considering θ of 0.05 as a common value for Pt. Notably, the experimentally derived critical switching current density J_c is 49 MA cm^{-2}. This discrepancy is reasonable because the simulation for SOT switching was performed at 0 K but the SOT experiments were carried out at 180 K. The coercive field under 0 K is simulated to be around 150 kOe while that for experimental sample is around 2.5 kOe at 180 K. It turns out that these unequal critical switching current density and coercive field for both experiments and simulations bring about a consistent $\mu_0 H_c/J_c$ of about 5 mT cm^2 MA^{-1}, which is higher than that of typical FM materials such as Pt/Co/AlO$_x$ (26, 52, 56).

<u>Text S4: General discussions about the influence of arbitrary orientations of p and H on 180º</u>
<u>switching</u> of the Néel vector

When d is perpendicular to the plane of m and n, all combinations of p and H along any direction in the $D(X)$-$N(Y)$-$M(Z)$ orthogonal coordinate system form a linear space. p or H along $D(X)$, $N(Y)$, or $M(Z)$ form 9 orthogonal bases of this linear space, denoted as (p_X, H_D), (p_X, H_Y), (p_X, H_M), (p_N, H_D), (p_N, H_Y), (p_N, H_M), (p_M, H_D), (p_M, H_Y), and (p_M, H_M), respectively (fig. S12A–I). Any $p \otimes H$ can be projected to these 9 bases.

Base2 of (p_X, H_Y), namely p parrel to $D(X)$ and H parrel to $N(Y)$ as we introduced in Fig. 3, is the only base that supports deterministic 180º switching of Néel vector. When the driven force (namely the damping-like effective field H_{DL}) is smaller than the low energy barrier from n_+ to n_- as shown in Fig. 3B, n cannot step over this energy barrier and thus settle at an intermediate state n' (fig. S12J). After SOT is turned off, n will return back to the initial direction. When H_{DL} is larger than the low energy barrier from n_+ to n_- but smaller than the high energy barrier from n_- to n_+, n can step over the low barrier and settle at an intermediate state n'_- (fig. S12K). After SOT is turned off, n will naturally relax to the local energy minimum n_- to achieve the deterministic 180º switching from n_+ to n_-. When H_{DL} is larger than the high energy barrier, n will be driven into continuous rotation (fig. S12L).

For other Bases, three requirements as we introduced cannot be fully met. For Base1, H is perpendicular to the easy plane of m, adding equal Zeeman energy to the transition from n_+ to n_- and time-reversal transition from n_- to n_+, and thus violating requirement (3). For Base3, H is parallel to m, which breaks the energy degeneracy between n_+ and n_-, and thus violating requirement (1). For Base4–6, p is parallel to n, and hence cannot generate T_{ex}, violating requirement (2). For Base7–9, p is parallel to m, which drives n to rotate in the DON plane. $m_1 \times m_2$ does not fix in the same direction, which leads to an increase of DMI energy proportional to $d \cdot (m_1 \times m_2)$. As a result, only base 2 fulfils all requirements. Therefore, the criteria for deterministic 180º switching of the Néel vector is that $p \otimes H$ is not linear independent with base2 of (p_X, H_Y). Namely, p cannot in the NOM plane and H cannot in the MOD plane, which is universal for all cAFM with DMI-induced intrinsic net moment to achieve deterministic 180º switching.

When d is not perpendicular to the plane of m and n, the conclusions are consistent with the above. Now, Z is still parallel to M, but there is an angle between X and D as well as Y and N (fig. S13A-B). Note that m is always perpendicular to d to gain minimum DMI energy. If we set Z direction to be parallel to m, X axis can be defined as perpendicular to the plane of m and n, and Y axis can be defined as perpendicular to the plane of m and d. In this case, p along X, N, or M and H along D, Y, or M can be used to construct 9 bases of arbitrary p and H. Similarly, only base2 of p parrel to X and H parrel to Y supports deterministic 180º switching of Néel vector, proving the criteria for 180º switching (p cannot in the NOM plane and H cannot in the MOD plane) still holds in this scenario (fig. S13C–F). For cAFM Mn_5Si_3, it is easy to be satisfied because n is not aligned in-plane to obtain non-zero σ_{xy}. To model our SOT switching experiments of in-plane current pulses with assistant field H along the same direction, namely p and H are perpendicular to each other, we set p along a low symmetry direction of (3, –1, 0) with perpendicular H along (1, 3, 0) to ensure genericity. As expected, deterministic 180º switching of Néel vector can be achieved (fig. S13G). Notably, the rotation plane of n (indicated by a pink circle) and the easy plane of m (indicated by a blue circle) no longer overlap, but remains perpendicular to p and perpendicular to d, respectively, which is universal for base2 whether or not d is perpendicular to the plane of m and n. Moreover, if p is in the NOM plane or H is in the MOD plane, deterministic 180º switching cannot be achieved because the criteria is violated (fig. S13H–I).

Text S5: Estimation of the critical switching current density J_C

To estimate the critical switching current density J_c flowing in the Pt layer of the Al_2O_3/Mn_5Si_3(6 nm)/Pt(10 nm) stack, we first measured the temperature-dependent resistivities of Mn_5Si_3 and Pt single layers, respectively. The total critical switching current flowing in the Al_2O_3/Mn_5Si_3(6 nm)/Pt(10 nm) stack I_c is defined as $I_c = (I_+ + I_-)/2$. Here I_+ (I_-) are the zero points of the switching loop for positive (negative) electrical pulses (fig. S18A). Considering the shunting effect, the ratio of the current flowing in the Pt layer I_{Pt} and the Mn_5Si_3 layer $I_{Mn_5Si_3}$ is estimated to be

$$I_{Pt}:I_{Mn_5Si_3} = \frac{R_{Mn_5Si_3}}{R_{Pt}} = \frac{\rho_{Mn_5Si_3}/t_{Mn_5Si_3}}{\rho_{Pt}/t_{Pt}},$$ where $R_{Mn_5Si_3(Pt)}$, $\rho_{Mn_5Si_3(Pt)}$, and $t_{Mn_5Si_3(Pt)}$ are the resistance,

resistivity, and the thickness of Mn_5Si_3 (Pt) layer (fig. S18B). Therefore, we determined the current

flowing in the Pt layer to be $I_{Pt} = \frac{\rho_{Mn_5Si_3} t_{Pt}}{\rho_{Mn_5Si_3} t_{Pt} + \rho_{Pt} t_{Mn_5Si_3}} I_c$. The critical switching current density J_c is

defined as the current density in the Pt layer, resulting in $J_c = I_{Pt}/wt_{Pt}$, where w is the width of the writing channels in the cross bars.

Text S6: Atomic spin simulations based on different system parameters

To check the robustness of our atomic spin simulations and exclude possible artifacts due to different choices of system parameters, we performed control simulations. As shown in fig. S19A, there are no essential differences between the simulated hysteresis of out-of-plane net moment m_z at 150 K with different random seeds, which influences the random-generated initial atomic spin configuration for simulation. Besides, the evolution of n driven by different length of electrical pulses were tested with the same p and H as in fig. S13G to model experimental conditions (fig. S19B-D). It turns out that the switching of n can be accomplished by the electrical pulse as short as 25 ps, which reflects the advantage of high operation speed for Mn_5Si_3 based AFM device due to its fast-switching dynamics.

Text S7: Influence of field-like spin-orbit torque on 180º switching of the Néel vector

We consider the influence of field-like spin-orbit torques by adding corresponding effective field H_{FL} as a term $|\gamma| m_{ip} \times H_{FL,ip}$. When increasing H_{DL}, the simulation results for H_{FL} from 0 to 10 kOe all change in turn from no switching, non-deterministic switching, deterministic switching, partial rotation to rotation, represented by 5 panels of different colors (fig. S20). With the increase of H_{FL}, the critical H_{DL} to achieve deterministic switching increases. Thus, H_{FL} has negative influence on 180º switching of the Néel vector.
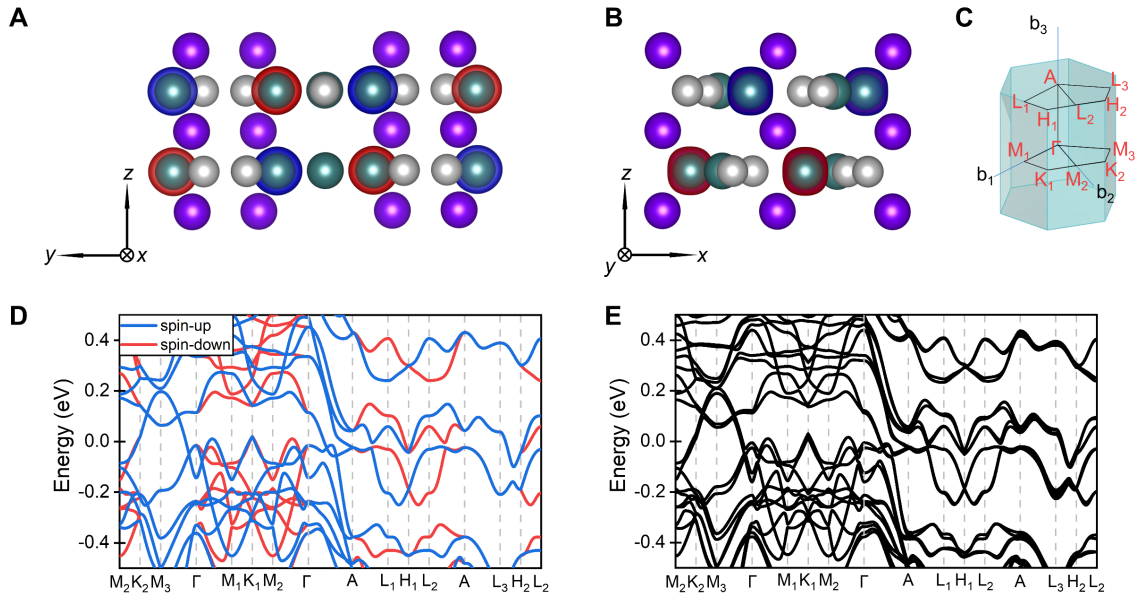
Fig. S1.
First-principles calculation of cAFM Mn₅Si₃. (A–B) Other perspectives of the crystal structure and magnetization density shown in Fig. 1A. (C) High symmetry points used for first-principles calculations. (D) DFT-calculated spin-splitting band structures of cAFM Mn_5Si_3 without and (E) with spin-orbit coupling.
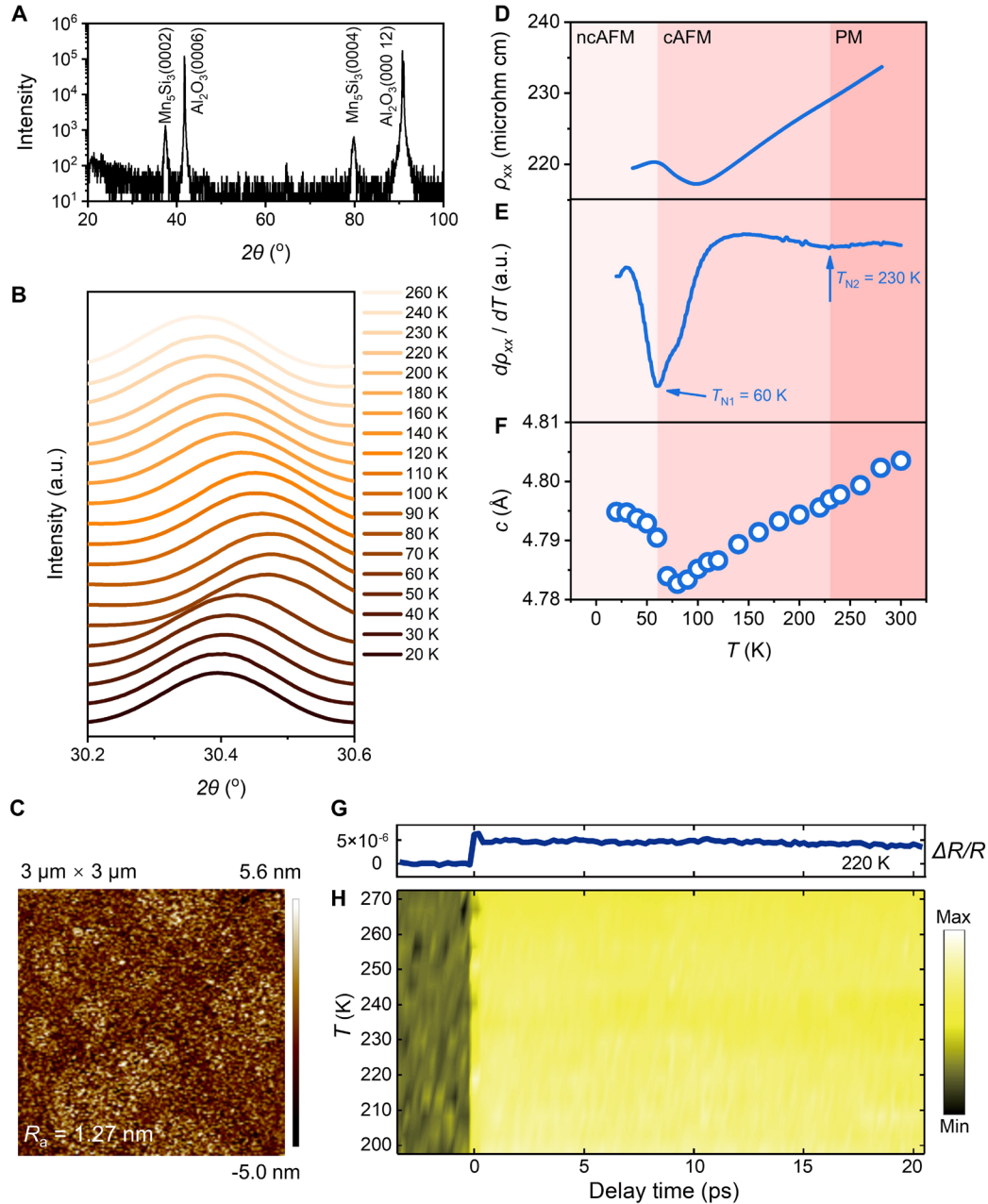
Fig. S2.

Basic characterizations of Mn₅Si₃ thin films. (**A**) XRD spectrum of Mn_5Si_3 film sputtered on $Al_2O_3(0001)$ substrate measured at room temperature with Cu K_α. (**B**) In-situ XRD spectra of the $Mn_5Si_3(0002)$ peak measured at low temperatures under X-ray from synchrotron radiation of 9.80 keV. (**C**) Atomic force microscopy image of $Mn_5Si_3(80$ nm) film. (**D**) Temperature-dependent longitudinal resistivity ρ_{xx}. (**E**) Temperature-derivative of longitudinal resistivity ρ_{xx}. (**F**) Temperature-dependent lattice parameter c extracted from (**B**). (**G**) Time-resolved reflectivity of Mn_5Si_3 thin film measured at 220 K. (**H**) 2D plot of the temperature-dependent time-resolved reflectivity between 200 K and 270 K with a step of 5 K.
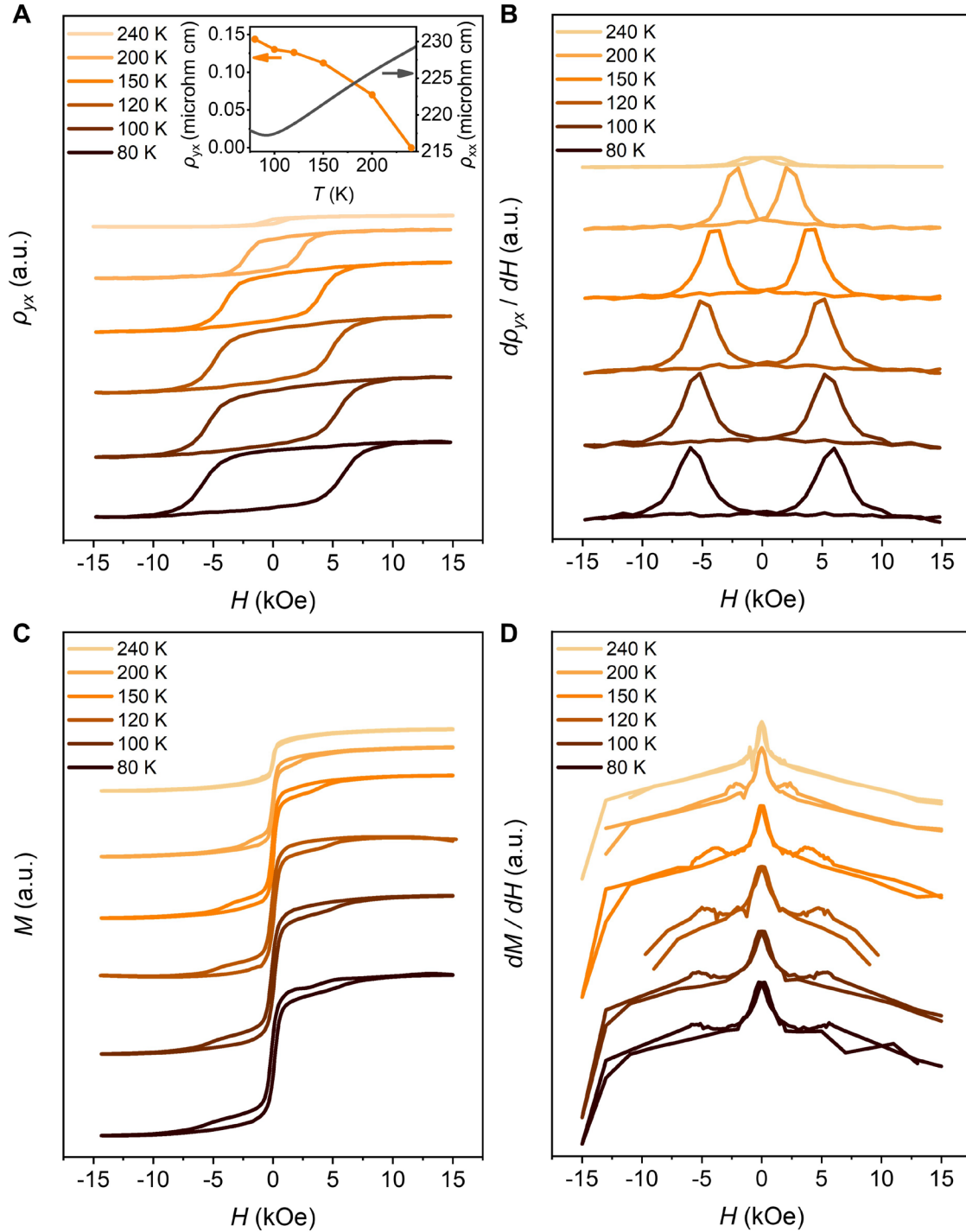
Fig. S3.
Hysteresis of Hall resistivity and corresponding magnetization of Mn₅Si₃ thin films. (A) ρ_{yx}-H curves and corresponding (**B**) Field-derivative curv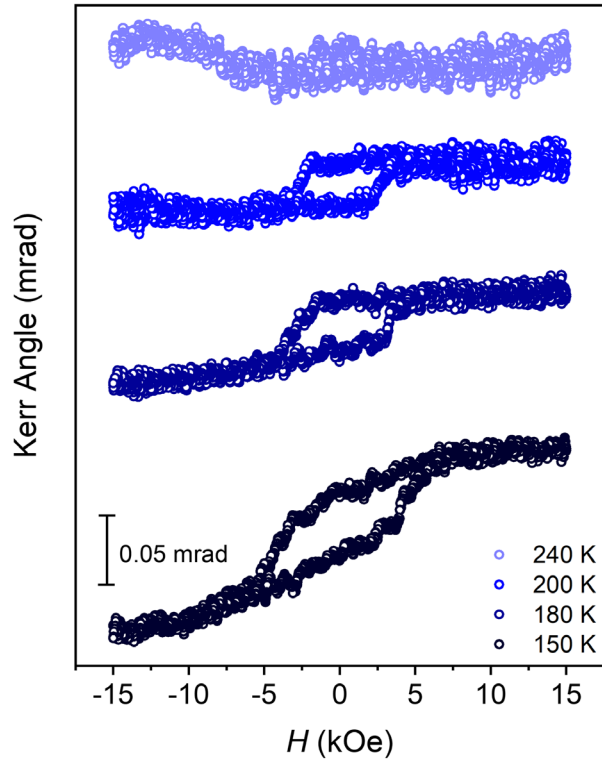es in logarithmic plot measured under different temperature. Inline image shows temperature dependences of ρ_{yx} and ρ_{xx}. (**c**) *M-H* curves and corresponding (**d**) Field-derivative curves in logarithmic plot measured under different temperatures.

Fig. S4.

Temperature-dependent polar magneto-optical Kerr effect measurements of Mn₅Si₃ thin film. The Kerr signal is rooted from the Hall conductance in light frequency, sharing similar origin of AHE in zero frequency limit.
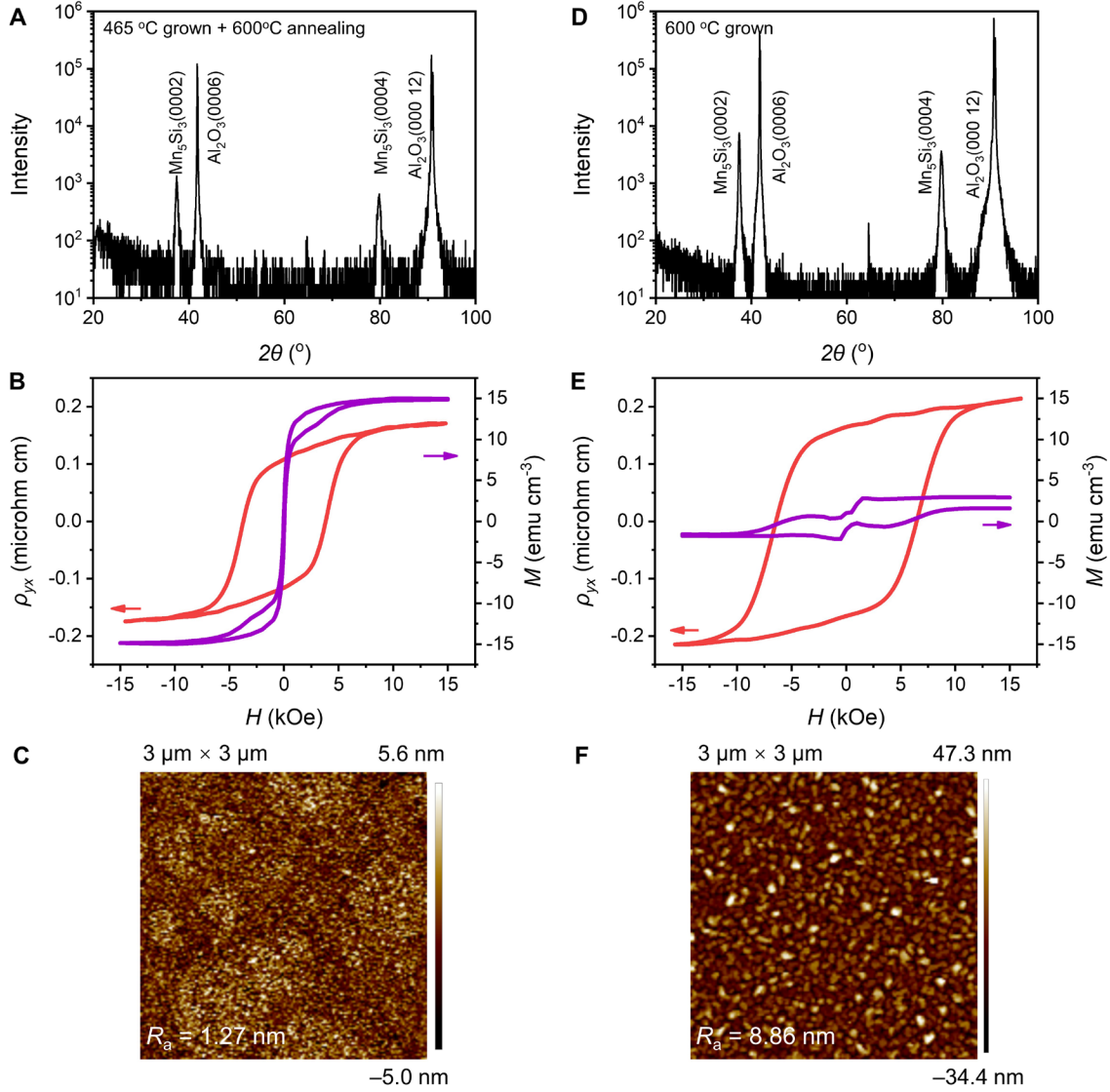
Fig. S5

Relationship between defect-induced net moment and crystallinity. (**A**, **D**) XRD spectra measured at room temperature with Cu K_α. (**B**, **E**) Hysteresis of Hall resistivity and corresponding magnetization measured at 150 K, and (**C**, **F**) Atomic force microscopy images of Mn_5Si_3(80 nm) thin films grown by different processes, respectively.
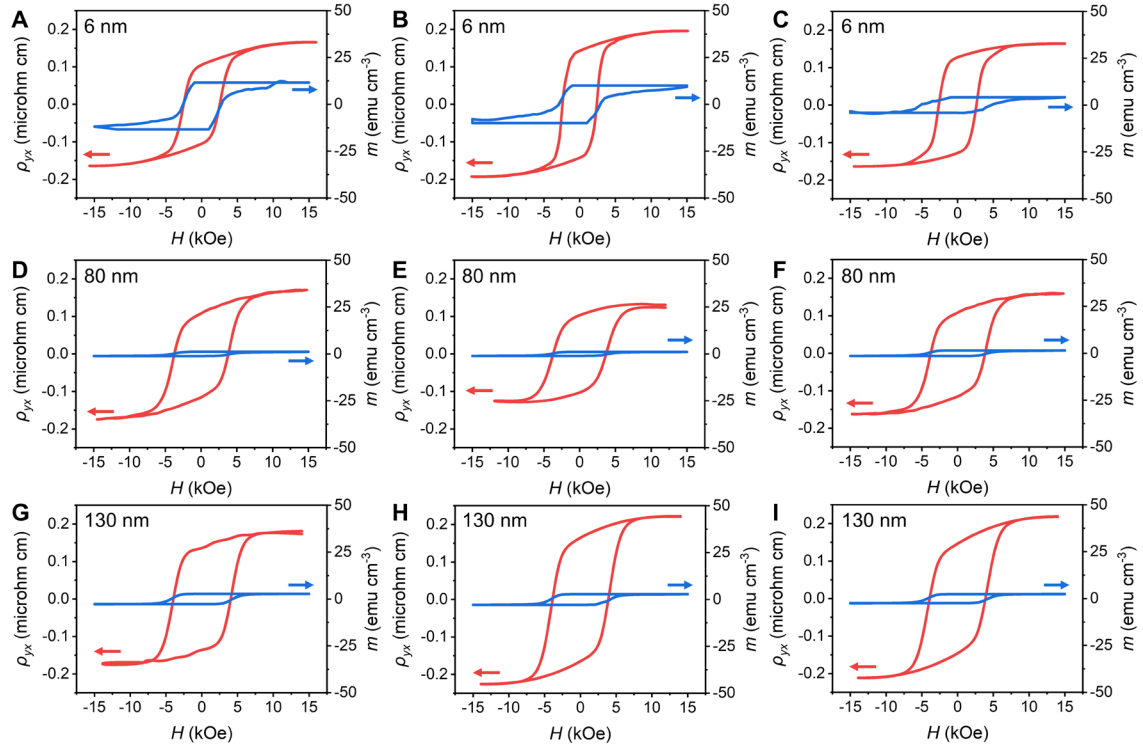
Fig. S6

Hysteresis of Hall resistivity and DMI-induced net moment m for Mn$_5$Si$_3$ thin film of different thickness. (**A**, **B**, **C**) Sample 1–3 of Mn$_5$Si$_3$(6 nm). (**D**, **E**, **F**) Sample 4–6 of Mn$_5$Si$_3$(80 nm). (**G**, **H**, **I**) Sample 7–9 of Mn$_5$Si$_3$(130 nm).
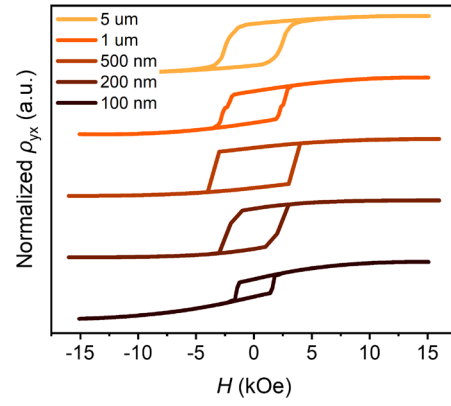
Fig. S7
Hall resistivity of Mn₅Si₃ with different channel width.
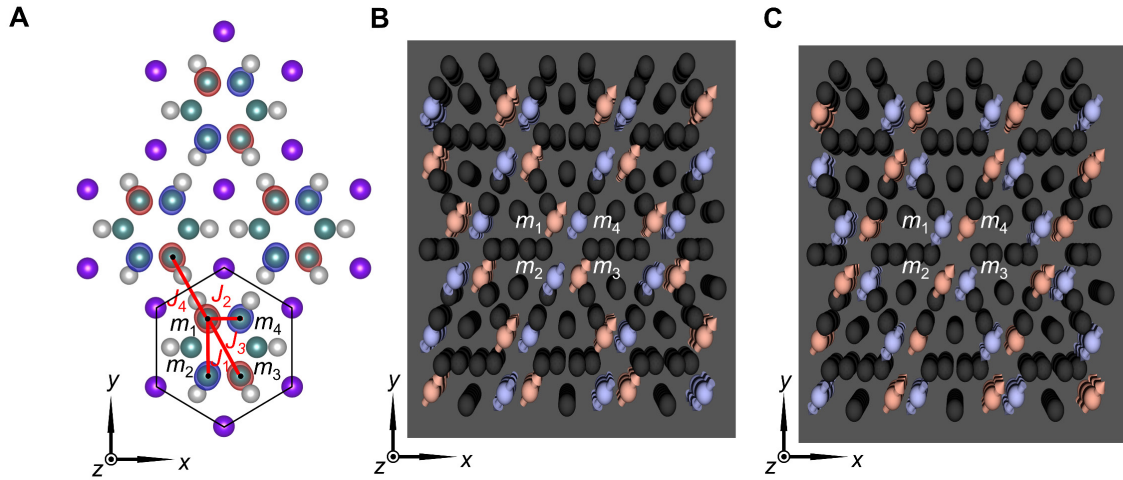
Fig. S8

Models and 3D visualizations for atomic spin simulations. (**A**) Magnetization density of cAFM Mn_5Si_3 with exchange interaction J_1, J_2, J_3, J_4 marked, which were used for simulations. (**B–C**) 3D visualization of the simulated 180° Néel vector switching results, where only a part of cells from the total $50 \times 50 \times 10$ cells used for simulations are shown to gain better visualization. The direction of atomic magnetic moment on magnetic Mn_b atoms is indicated by arrows, where red represents positive z-component and blue represents negative z-component.
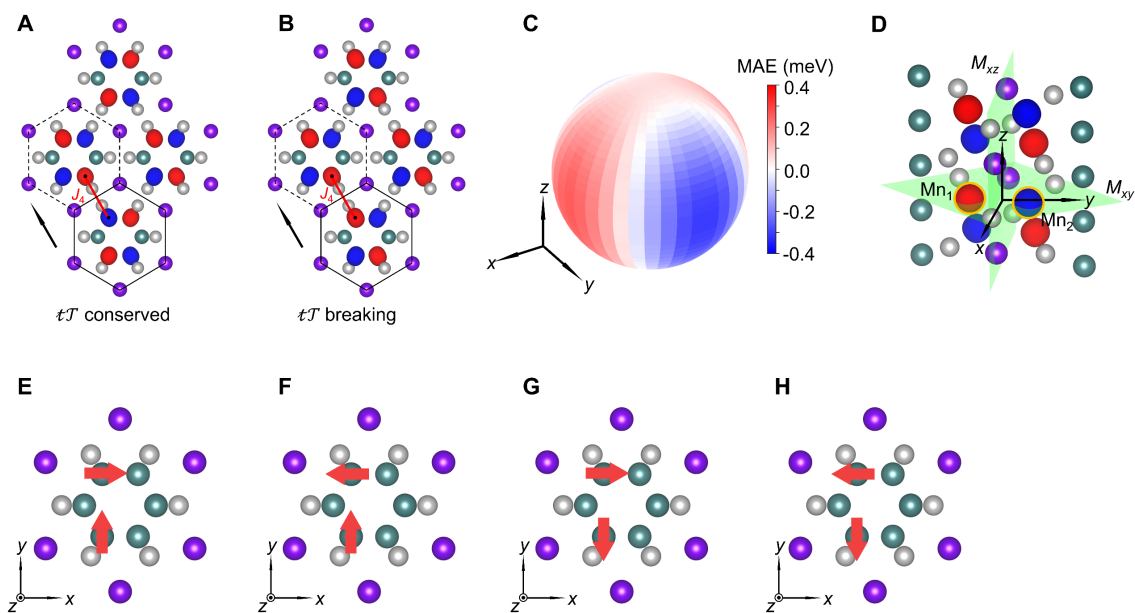
Fig. S9

Models for determining key parameters related to simulation and calculation. Crystal structure and magnetization density for (**A**) AFM J_4 and (**B**) FM J_4, where red and blue isosurfaces represent opposite magnetization density. The *xyz* Cartesian coordinate system is the same as Fig. 1A. (**C**) MAE for the Néel vector n along different orientations in the cartesian coordinate system compared with the case of n orienting to (1,1,1). (**D**) Schematic of the mirror planes in ideal single crystal Mn_5Si_3. (**E**–**H**) Schematics of spin configurations for DMI estimation.
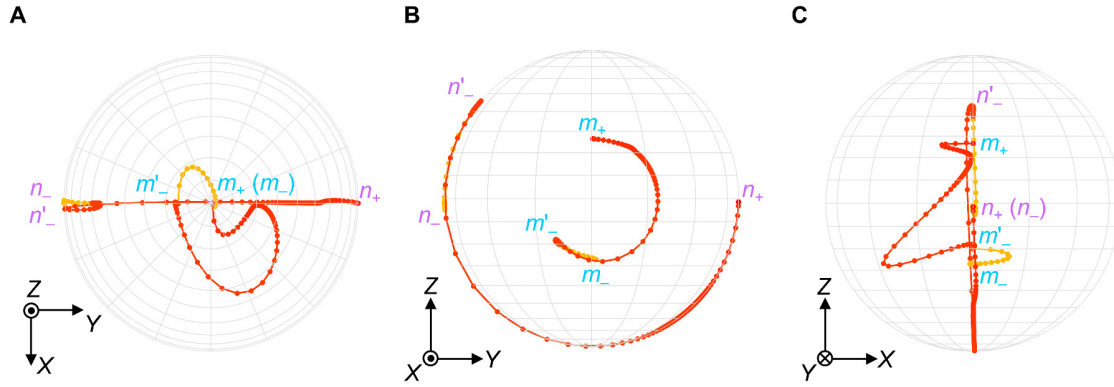
Fig. S10
Different projections of simulated 180º switching of the Néel vector by SOT shown in Fig. 3C. (**A**) Projection from +Z direction. (**B**) Projection from +X direction. (**C**) Projection from −Y direction. The rotation plane of n and the easy plane of m are both the *YOZ* plane. The trajectories of n are limited in the *YOZ* plane. The initial direction of m_+, the stable intermediate state of m'_- under SOT, and the 180º-reversed direction of m_- are all locate in the *YOZ* plane, though the transitions between them are flexible.
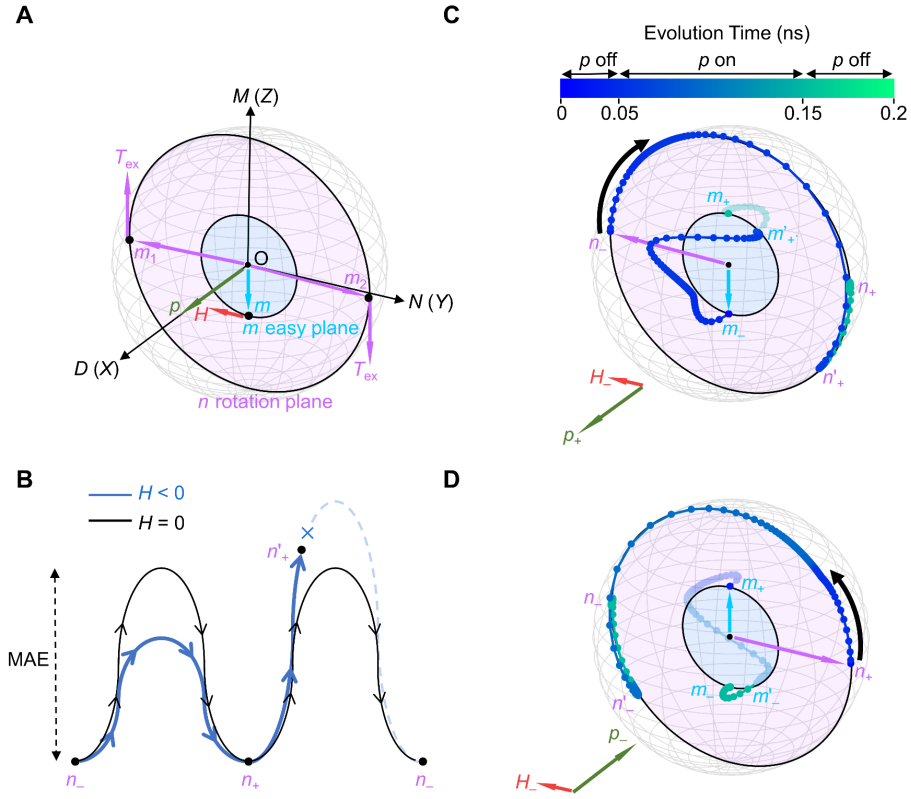
Fig. S11

180º switching of the Néel vector by SOT under negative magnetic field. (**A**) Schematic of n rotation driven by exchange torques T_{ex} with p along $+X$ and n along $-Y$. n can be simplified as $(m_1-m_2)/2$ for cAFM Mn_5Si_3 with four sublattices where $m_1 = m_3$ and $m_2 = m_4$ (Materials and Methods). The rotation of n is accompanied by the motion of m, which is favored by H along $-Y$. (**B**) Schematic of energy barriers for the transition from n_- to n_+ and n_+ to n_-. Without H, these two energy barriers are the same, determined by MAE. With $H < 0$, the degeneracy between them can be lifted. (**C**) Simulated switching trajectories of m and n for positive p_+ and negative H_- as well as (**D**) negative p_- and negative H_-. m is magnified 10 times for better visualization. The color of trajectories indicates the evolution time, where p is added from 0.05 ns to 0.15 ns.
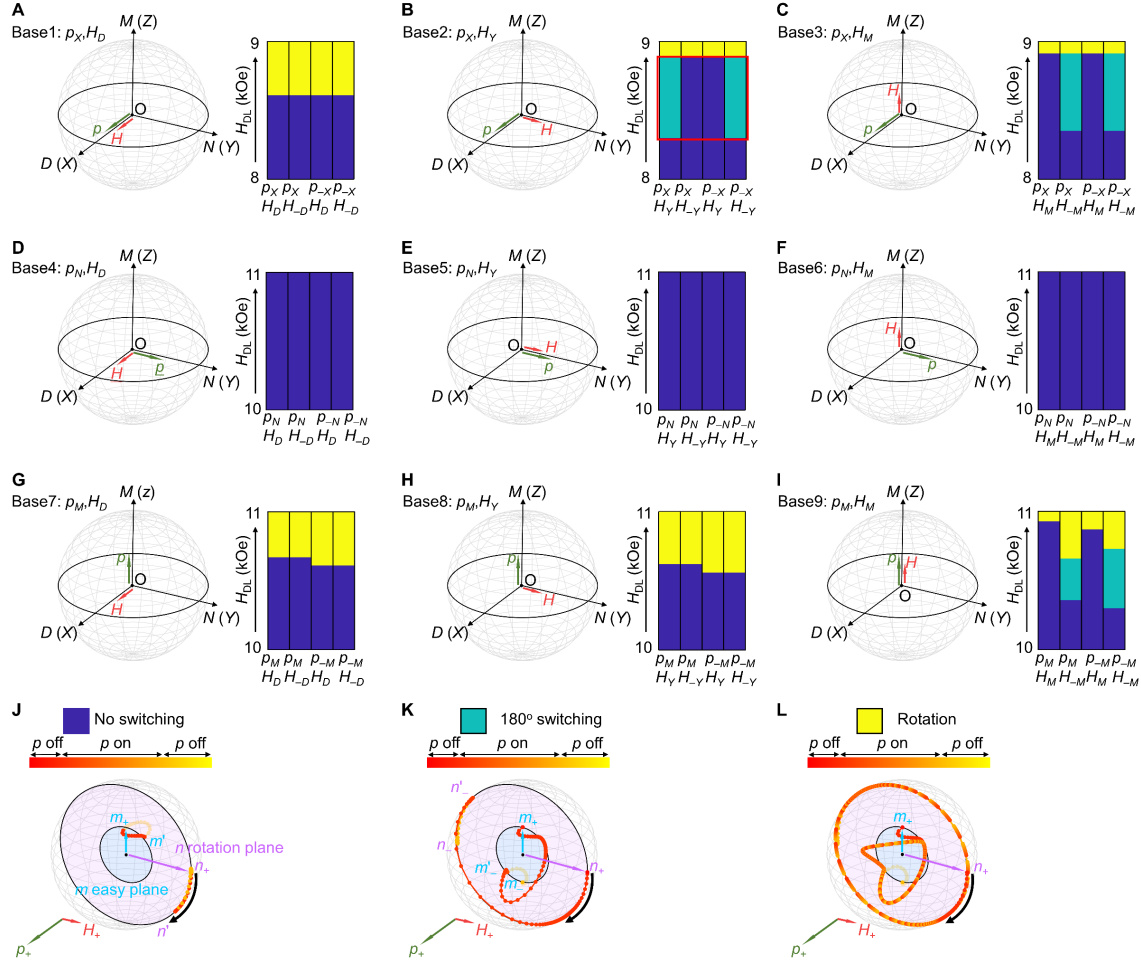
Fig. S12

Simulated 180º switching of the Néel vector by SOT under different bases of the *D(X)-N(Y)-M(Z)* orthogonal coordinate system (**A–I**) 9 bases of *p* and *H* for the *D(X)-N(Y)-M(Z)* orthogonal coordinate system. The simulation results of SOT switching for each base under different polarity combinations of *p* and *H* with different magnitudes of the damping-like effective field H_{DL} are included at the right side, where blue, green, and yellow panels represent different simulation results of no switching, 180º switching, and rotation, respectively. Base2 is the only base that supports deterministic 180º switching of Néel vector, which is circled by a red square in (**B**). Representative trajectories of *m* and *n* with positive p_+ and positive H_+ for base2, corresponding to simulation results of (**J**) no switching under H_{DL} of 8.0 kOe, (**K**) 180º switching under H_{DL} of 8.5 kOe, and (**L**) Rotation under H_{DL} of 9.0 kOe, respectively.
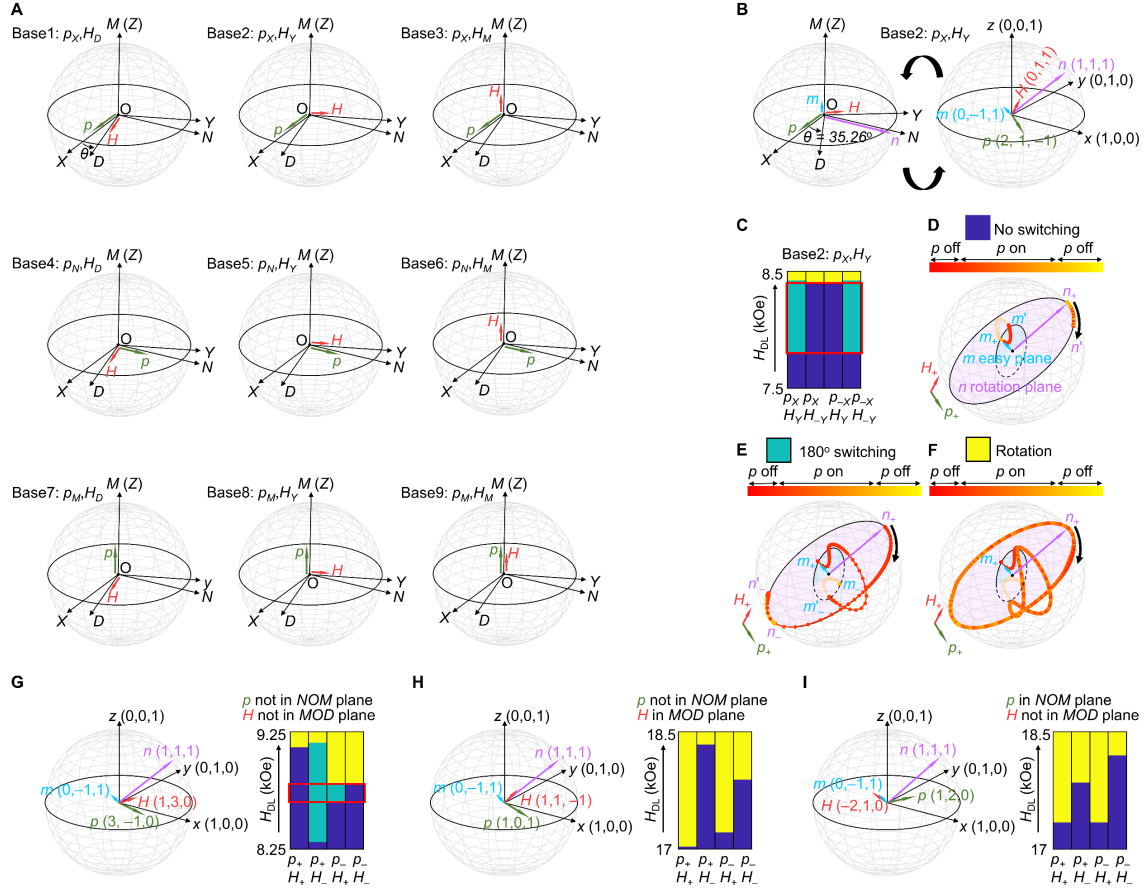
Fig. S13

Simulated 180° switching of the Néel vector by SOT when *d* is not perpendicular to the plane of *m* and *n*. (**A**) 9 bases of *p* and *H* when *d* is not perpendicular to the plane of *m* and *n*. (**B**) The interconversion of *D-N-M* coordinate system with Cartesian coordinate system *xyz* as we defined in Fig. 1 and Fig. 2. Take *n* along (1, 1, 1) in the *xyz* coordinate system as an example, the angle θ between *X* axis and *D* axis is 35.26° if considering *d* along *x* for simplicity without loss of genericity, with all of directions of *m*, *n*, *p*, and *H* marked for base2. (**C**) The simulation results of SOT switching for base2 under different polarity combinations of *p* and *H* with different magnitudes of the damping-like effective field H_{DL}, where blue, green, and yellow panels represent different simulation results of no switching, 180° switching, and rotation, respectively. Base2 is the only base that supports deterministic 180° switching of Néel vector, which is circled by a red square. Representative trajectories of *m* and *n* under positive p_+ and positive H_+ for base2, corresponding to simulation results of (**D**) no switching, (**E**) 180° switching, and (**F**) Rotation, respectively. These trajectories are similar to that of fig. S12J–L for *d* perpendicular to the plane of *m* and *n*, (**G**) Representative simulation results of SOT switching for *p* along (3, –1,0) and *H* along (1, 3, 0), (**H**) *p* along (1, 0, 1) and *H* along (1, 1, –1), and (**I**) *p* along (1, 2, 0) and *H* along (–2, 1, 0) under different polarity combinations of *p* and *H* with different magnitudes of H_{DL}. Deterministic 180° switching of Néel vector can be achieved when *p* is not in the *NOM* plane and *H* is not in the *MOD* plane, but cannot be achieved when *p* is in the *NOM* plane or *H* is in the *MOD* plane.
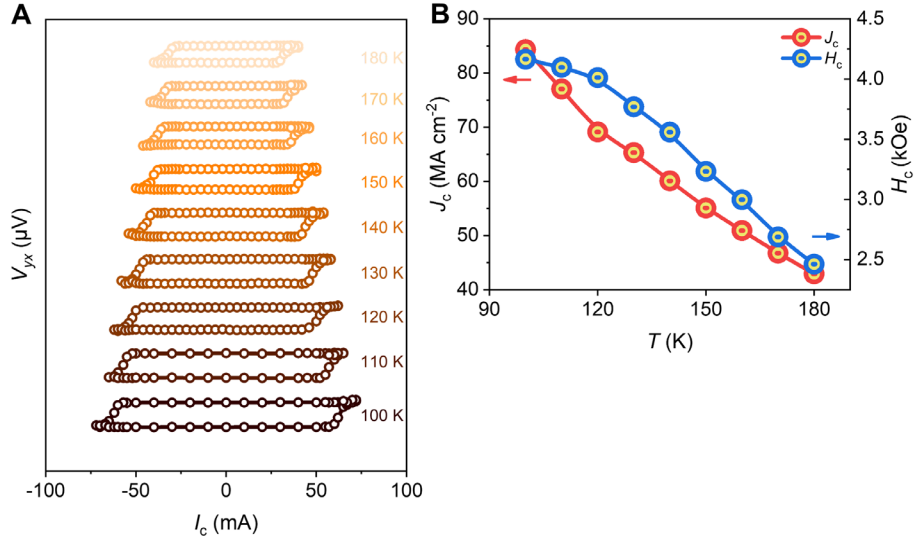
Fig. S14
180° electrical switching of cAFM Mn₅Si₃ under different temperatures. (**A**) Temperature-dependent SOT switching of cAFM Mn_5Si_3 under 0.2 kOe assistant field. (**B**) Critical switching current density J_c extracted from (**A**) with corresponding coercive field H_c of the AHE. H_c increases as temperature decreases, indicating that the uniaxial anisotropy is increasing, resulting in the increase of J_c.
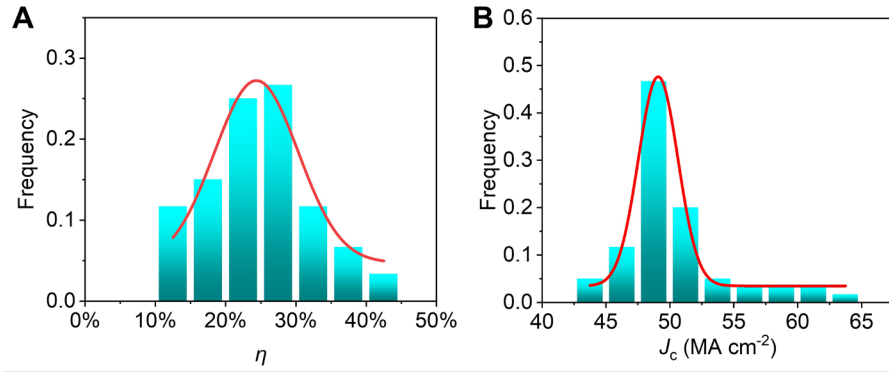
Fig. S15

Switching ratio η and critical switching current density J_c for 60 devices. (**A**) η and (**B**) J_c follow normal distribution that average at 24% and 49 MA cm^{-2} with the standard deviation σ of 12% and 3 MA cm^{-2}, respectively.
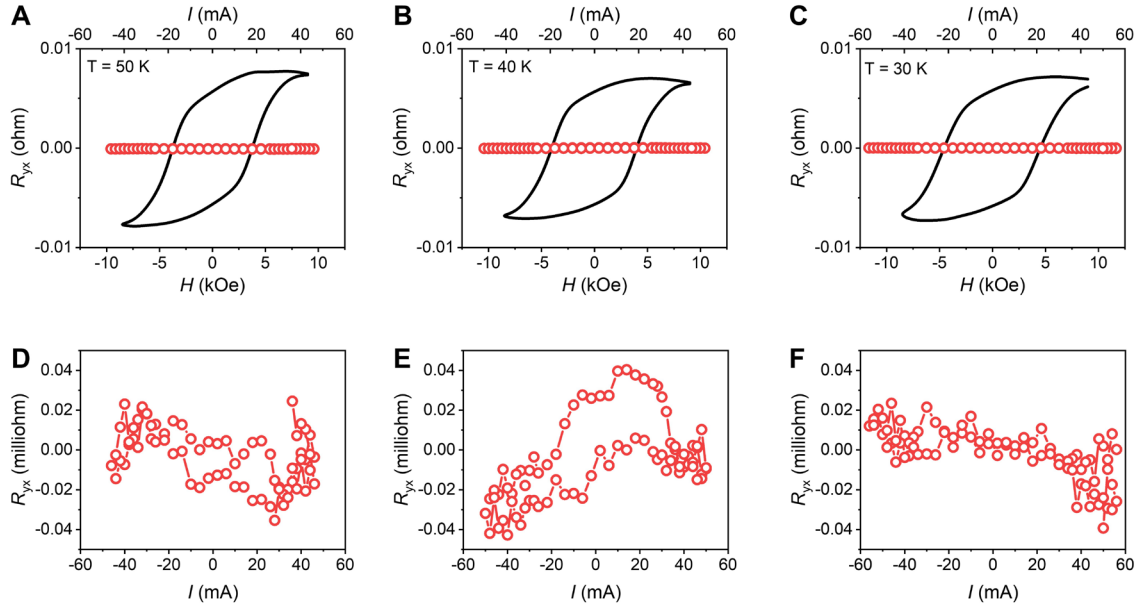
Fig. S16

No electrical switching of ncAFM Mn₅Si₃. **(A–C)** Hall resistance R_{yx} collected when sweeping electrical pulses with assistant field H of 0.2 kOe (red dot) and R_{yx} collected when sweeping out-of-plane magnetic field (black line). **(D–F)** Magnified images of Hall resistance R_{yx} variation under electrical pulses in **(A–C)**, where no switching can be observed.
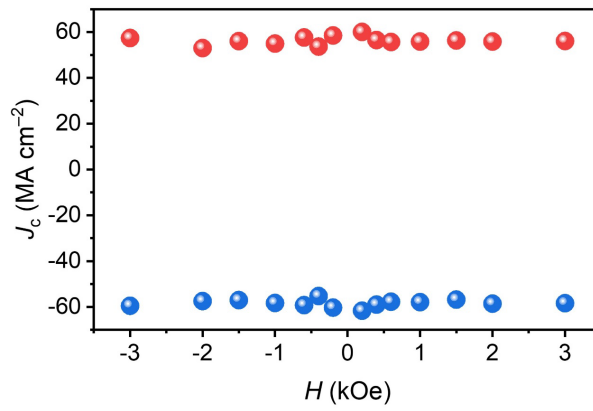
Fig. S17

Critical switching current density J_c under different assistant field H at 180 K for another sample.
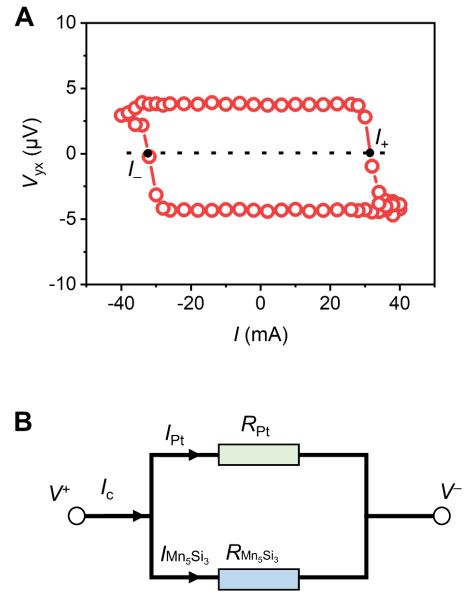
Fig. S18
Schematic for determining the critical switching current density J_c. (A) Extraction of I_+ and I_- from the switching loop. **(B)** Equivalent circuit of the shunting effect in the $Al_2O_3/Mn_5Si_3/Pt$ stack.
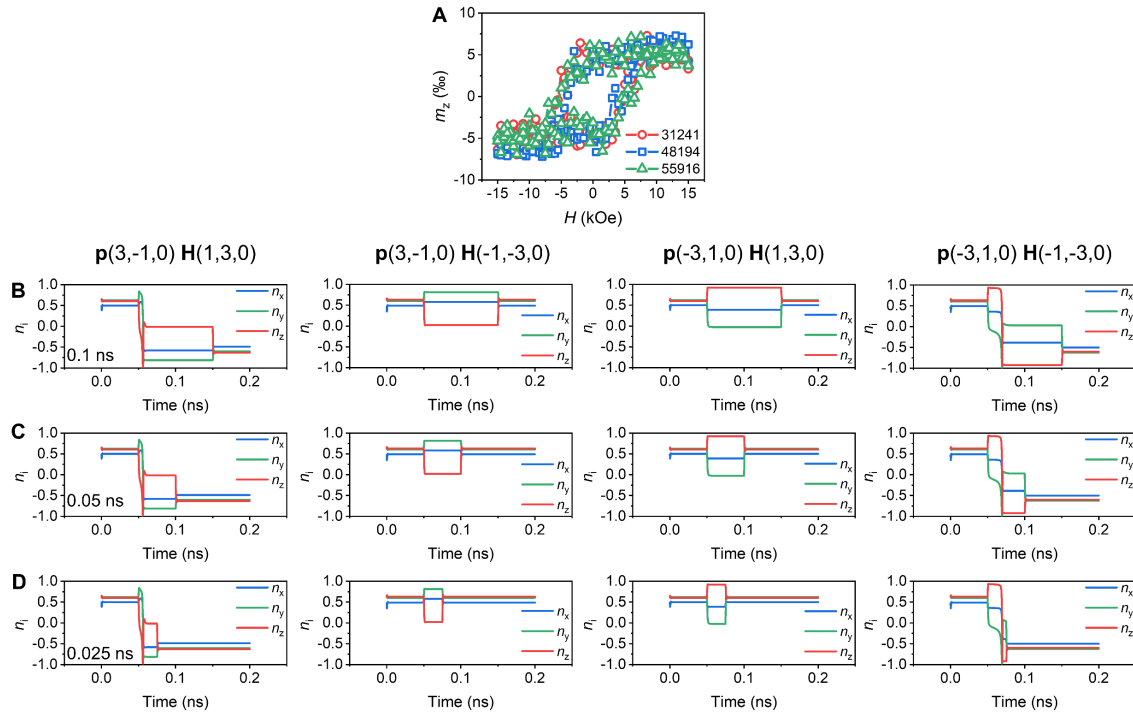
Fig. S19

Atomic spin simulations of magnetic hysteresis and SOT switching based on different system parameters. (**A**) Simulated hysteresis of out-of-plane net moment m_z under at 150 K with different random seeds. (**B–D**) Simulated evolution of n for different pulse lengths under different polarity combinations of p and H with H_{DL} of 8.7 kOe. The pulse is added at 0.05 ns for each simulation.
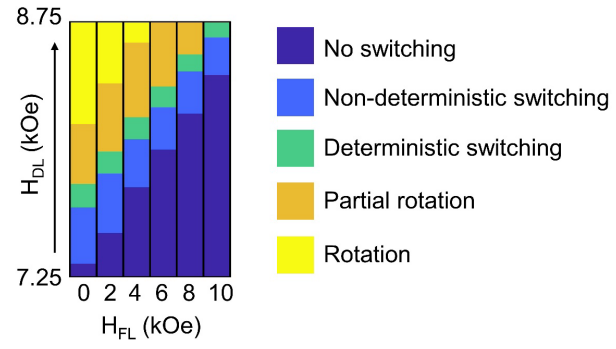
Fig. S20

Atomic spin simulations considering both damping-like effective field H_{DL} and field-like effective field H_{FL}.

Movie S1.

A movie was made from the simulated 180° switching of atomic magnetic moments of Mn_5Si_3 under different polarity combinations of p and H with H_{DL} of 8.7 kOe, consistent with the settings in fig. S13G to model experimental conditions. $p(3,-1,0)H(1,3,0)$ and $p(-3, 1,0)H(-1,-3,0)$ switch n from $n_+(1,1,1)$ to $n_-(-1,-1,-1)$ while $p(3,-1,0)H(-1,-3,0)$ and $p(-3,1,0)H(1,3,0)$ switch n from $n_-(-1,-1,-1)$ to $n_+(1,1,1)$. The electrical pulse of 0.1 ns is started at 50 s and ended at 2min30s in the movie.

REFERENCES AND NOTES

1. S. A. Wolf, D. D. Awschalom, R. A. Buhrman, J. M. Daughton, S. von Molnár, M. L. Roukes, A. Y. Chtchelkanova, D. M. Treger, Spintronics: A spin-based electronics vision for the future. *Science* **294**, 1488–1495 (2001).

2. S. Bhatti, R. Sbiaa, A. Hirohata, H. Ohno, S. Fukami, S. N. Piramanayagam, Spintronics based random access memory: A review. *Mater. Today* **20**, 530–548 (2017).

3. C. Song, R. Q. Zhang, L. Y. Liao, Y. J. Zhou, X. F. Zhou, R. Y. Chen, Y. F. You, X. Z. Chen, F. Pan, Spin-orbit torques: Materials, mechanisms, performances, and potential applications. *Prog. Mater. Sci.* **118**, 100761 (2021).

4. M. Julliere, Tunneling between ferromagnetic films. *Phys. Lett.* **54**, 225–226 (1975).

5. T. Miyazaki, N. Tezuka, Giant magnetic tunneling effect in $Fe/Al_2O_3/Fe$ junction. *J. Magn. Magn. Mater.* **139**, L231-L234 (1995).

6. J. S. Moodera, L. R. Kinder, T. M. Wong, R. Meservey, Large magnetoresistance at room temperature in ferromagnetic thin film tunnel junctions. *Phys. Rev. Lett.* **74**, 3273–3276 (1995).

7. J. C. Slonczewski, Current-driven excitation of magnetic multilayers. *J. Magn. Magn. Mater.* **159**, L1-L7 (1996).

8. L. Berger, Emission of spin waves by a magnetic multilayer traversed by a current. *Phys. Rev. B* **54**, 9353–9358 (1996).

9. I. M. Miron, K. Garello, G. Gaudin, P.-J. Zermatten, M. V. Costache, S. Auffret, S. Bandiera, B. Rodmacq, A. Schuhl, P. Gambardella, Perpendicular switching of a single ferromagnetic layer induced by in-plane current injection. *Nature* **476**, 189–193 (2011).

10. L. Liu, C.-F. Pai, Y. Li, H. W. Tseng, D. C. Ralph, R. A. Buhrman, Spin-torque switching with the giant spin Hall effect of tantalum. *Science* **336**, 555–558 (2012).

11. T. Jungwirth, X. Marti, P. Wadley, J. Wunderlich, Antiferromagnetic spintronics. *Nat. Nanotechnol.* **11**, 231–241 (2016).

12. V. Baltz, A. Manchon, M. Tsoi, T. Moriyama, T. Ono, Y. Tserkovnyak, Antiferromagnetic spintronics. *Rev. Mod. Phys.* **90**, (2018).

13. P. Wadley, B. Howells, J. Zelezny, C. Andrews, V. Hills, R. P. Campion, V. Novak, K. Olejnik, F. Maccherozzi, S. S. Dhesi, S. Y. Martin, T. Wagner, J. Wunderlich, F. Freimuth, Y. Mokrousov, J. Kunes, J. S. Chauhan, M. J. Grzybowski, A. W. Rushforth, K. W. Edmonds, B. L. Gallagher, T. Jungwirth, Electrical switching of an antiferromagnet. *Science* **351**, 587–590 (2016).

14. P. Vaidya, S. A. Morley, J. van Tol, Y. Liu, R. Cheng, A. Brataas, D. Lederman, E. del Barco, Subterahertz spin pumping from an insulating antiferromagnet. *Science* **368**, 160–165 (2020).

15. B. G. Park, J. Wunderlich, X. Martí, V. Holý, Y. Kurosaki, M. Yamada, H. Yamamoto, A. Nishide, J. Hayakawa, H. Takahashi, A. B. Shick, T. Jungwirth, A spin-valve-like magnetoresistance of an antiferromagnet-based tunnel junction. *Nat. Mater.* **10**, 347–351 (2011).

16. Y. Y. Wang, C. Song, B. Cui, G. Y. Wang, F. Zeng, F. Pan, Room-temperature perpendicular exchange coupling and tunneling anisotropic magnetoresistance in an antiferromagnet-based tunnel junction. *Phys. Rev. Lett.* **109**, 137201 (2012).

17. X. Marti, I. Fina, C. Frontera, J. Liu, P. Wadley, Q. He, R. J. Paull, J. D. Clarkson, J. Kudrnovský, I. Turek, J. Kuneš, D. Yi, J. H. Chu, C. T. Nelson, L. You, E. Arenholz, S. Salahuddin, J. Fontcuberta, T. Jungwirth, R. Ramesh, Room-temperature antiferromagnetic memory resistor. *Nat. Mater.* **13**, 367–374 (2014).

18. D.-F. Shao, S.-H. Zhang, M. Li, C.-B. Eom, E. Y. Tsymbal, Spin-neutral currents for spintronics. *Nat. Commun.* **12**, 7061 (2021).

19. L. Šmejkal, A. B. Hellenes, R. González-Hernández, J. Sinova, T. Jungwirth, Giant and tunneling magnetoresistance in unconventional collinear antiferromagnets with nonrelativistic spin-momentum coupling. *Phys. Rev. X* **12**, 011028 (2022).

20. P. Qin, H. Yan, X. Wang, H. Chen, Z. Meng, J. Dong, M. Zhu, J. Cai, Z. Feng, X. Zhou, L. Liu, T. Zhang, Z. Zeng, J. Zhang, C. Jiang, Z. Liu, Room-temperature magnetoresistance in an all-antiferromagnetic tunnel junction. *Nature* **613**, 485–489 (2023).

21. X. Chen, T. Higo, K. Tanaka, T. Nomoto, H. Tsai, H. Idzuchi, M. Shiga, S. Sakamoto, R. Ando, H. Kosaki, T. Matsuo, D. Nishio-Hamane, R. Arita, S. Miwa, S. Nakatsuji, Octupole-driven magnetoresistance in an antiferromagnetic tunnel junction. *Nature* **613**, 490–495 (2023).

22. S. Y. Bodnar, L. Smejkal, I. Turek, T. Jungwirth, O. Gomonay, J. Sinova, A. A. Sapozhnik, H. J. Elmers, M. Klaui, M. Jourdan, Writing and reading antiferromagnetic Mn_2Au by Néel spin-orbit torques and large anisotropic magnetoresistance. *Nat. Commun.* **9**, 348 (2018).

23. X. Z. Chen, R. Zarzuela, J. Zhang, C. Song, X. F. Zhou, G. Y. Shi, F. Li, H. A. Zhou, W. J. Jiang, F. Pan, Y. Tserkovnyak, Antidamping-torque-induced switching in biaxial antiferromagnetic insulators. *Phys. Rev. Lett.* **120**, 207204 (2018).

24. Y. Cheng, S. Yu, M. Zhu, J. Hwang, F. Yang, Electrical switching of tristate antiferromagnetic Néel order in α−Fe2O3 epitaxial films. *Phys. Rev. Lett.* **124**, 027202 (2020).

25. J. Godinho, H. Reichlova, D. Kriegner, V. Novak, K. Olejnik, Z. Kaspar, Z. Soban, P. Wadley, R. P. Campion, R. M. Otxoa, P. E. Roy, J. Zelezny, T. Jungwirth, J. Wunderlich, Electrically induced and detected Néel vector reversal in a collinear antiferromagnet. *Nat. Commun.* **9**, 4686 (2018).

26. T. Higo, K. Kondou, T. Nomoto, M. Shiga, S. Sakamoto, X. Chen, D. Nishio-Hamane, R. Arita, Y. Otani, S. Miwa, S. Nakatsuji, Perpendicular full switching of chiral antiferromagnetic order by current. *Nature* **607**, 474–479 (2022).

27. J.-Y. Yoon, P. Zhang, C.-T. Chou, Y. Takeuchi, T. Uchimura, J. T. Hou, J. Han, S. Kanai, H. Ohno, S. Fukami, L. Liu, Handedness anomaly in a non-collinear antiferromagnet under spin–orbit torque. *Nat. Mater.* **22**, 1106–1113 (2023).

28. Z. Feng, X. Zhou, L. Šmejkal, L. Wu, Z. Zhu, H. Guo, R. González-Hernández, X. Wang, H. Yan, P. Qin, X. Zhang, H. Wu, H. Chen, Z. Meng, L. Liu, Z. Xia, J. Sinova, T. Jungwirth, Z. Liu, An anomalous Hall effect in altermagnetic ruthenium dioxide. *Nat. Electron.* **5**, 735–743 (2022).

29. I. Kounta, H. Reichlova, D. Kriegner, R. Lopes Seeger, A. Bad'ura, M. Leiviska, A. Boussadi, V. Heresanu, S. Bertaina, M. Petit, E. Schmoranzerova, L. Smejkal, J. Sinova, T. Jungwirth, V. Baltz, S. T. B. Goennenwein, L. Michez, Competitive actions of MnSi in the epitaxial growth of Mn5Si3 thin films on Si(111). *Phys. Rev. Mater.* **7**, 024416 (2023).

30. R. D. Gonzalez Betancourt, J. Zubac, R. Gonzalez-Hernandez, K. Geishendorf, Z. Soban, G. Springholz, K. Olejnik, L. Smejkal, J. Sinova, T. Jungwirth, S. T. B. Goennenwein, A. Thomas, H. Reichlova, J. Zelezny, D. Kriegner, Spontaneous anomalous Hall effect arising from an unconventional compensated magnetic phase in a semiconductor. *Phys. Rev. Lett.* **130**, 036702 (2023).

31. L. Šmejkal, A. H. MacDonald, J. Sinova, S. Nakatsuji, T. Jungwirth, Anomalous Hall antiferromagnets. *Nat. Rev. Mater.* **7**, 482–496 (2022).

32. L. Šmejkal, R. González-Hernández, T. Jungwirth, J. Sinova, Crystal time-reversal symmetry breaking and spontaneous Hall effect in collinear antiferromagnets. *Sci. Adv.* **6**, eaaz8809 (2020).

33. M. Naka, S. Hayami, H. Kusunose, Y. Yanagi, Y. Motome, H. Seo, Spin current generation in organic antiferromagnets. *Nat. Commun.* **10**, 4305 (2019).

34. K.-H. Ahn, A. Hariki, K.-W. Lee, J. Kuneš, Antiferromagnetism inRuO2asd-wave pomeranchuk instability. *Phys. Rev. B* **99**, 184432 (2019).

35. L.-D. Yuan, Z. Wang, J.-W. Luo, E. I. Rashba, A. Zunger, Giant momentum-dependent spin splitting in centrosymmetric low-Z antiferromagnets. *Phys. Rev. B* **102**, 014422 (2020).

36. R. Gonzalez-Hernandez, L. Smejkal, K. Vyborny, Y. Yahagi, J. Sinova, T. Jungwirth, J. Zelezny, Efficient electrical spin splitter based on nonrelativistic collinear antiferromagnetism. *Phys. Rev. Lett.* **126**, 127701 (2021).

37. H. Y. Ma, M. Hu, N. Li, J. Liu, W. Yao, J. F. Jia, J. Liu, Multifunctional antiferromagnetic materials with giant piezomagnetism and noncollinear spin current. *Nat. Commun.* **12**, 2846 (2021).

38. L. Šmejkal, J. Sinova, T. Jungwirth, Beyond conventional ferromagnetism and antiferromagnetism: A phase with nonrelativistic spin and crystal rotation symmetry. *Phys. Rev. X* **12**, 031042 (2022).

39. L. Šmejkal, J. Sinova, T. Jungwirth, Emerging research landscape of altermagnetism. *Phys. Rev. X* **12**, 040501 (2022).

40. A. Bose, N. J. Schreiber, R. Jain, D.-F. Shao, H. P. Nair, J. Sun, X. S. Zhang, D. A. Muller, E. Y. Tsymbal, D. G. Schlom, D. C. Ralph, Tilted spin current generated by the collinear antiferromagnet ruthenium dioxide. *Nat. Electron.* **5**, 267–274 (2022).

41. H. Bai, L. Han, X. Y. Feng, Y. J. Zhou, R. X. Su, Q. Wang, L. Y. Liao, W. X. Zhu, X. Z. Chen, F. Pan, X. L. Fan, C. Song, Observation of spin splitting torque in a collinear antiferromagnet$RuO2$. *Phys. Rev. Lett.* **128**, 197202 (2022).

42. S. Karube, T. Tanaka, D. Sugawara, N. Kadoguchi, M. Kohda, J. Nitta, Observation of spin-splitter torque in collinear antiferromagnetic$RuO2$. *Phys. Rev. Lett.* **129**, 137201 (2022).

43. P. J. Brown, J. B. Forsyth, V. Nunez, F. Tasset, The low-temperature antiferromagnetic structure of $Mn5Si3$revised in the light of neutron polarimetry. *J. Phys. Condens. Matter* **4**, 10025 (1992), 10036.

44. P. Brown, J. Forsyth, Antiferromagnetism in Mn_5Si_3: The magnetic structure of the AF2 phase at 70 K. *J. Phys. Condens. Matter* **7**, 7619– 7628 (1995).

45. M. Gottschilch, O. Gourdon, J. Persson, C. de la Cruz, V. Petricek, T. Brueckel, Study of the antiferromagnetism of Mn_5Si_3: An inverse magnetocaloric effect material. *J. Mater. Chem.* **22**, 15275–15284 (2012).

46. C. Surgers, G. Fischer, P. Winkel, H. V. Lohneysen, Large topological Hall effect in the non-collinear phase of an antiferromagnet. *Nat. Commun.* **5**, 3400 (2014).

47. N. Biniskos, K. Schmalzl, S. Raymond, S. Petit, P. Steffens, J. Persson, T. Bruckel, Spin fluctuations drive the inverse magnetocaloric effect in $Mn5Si3$. *Phys. Rev. Lett.* **120**, 257205 (2018).

48. I. Dzyaloshinsky, A thermodynamic theory of "weak" ferromagnetism of antiferromagnetics. *J. Phys. Chem. Solid* **4**, 241–255 (1958).

49. N. Nagaosa, J. Sinova, S. Onoda, A. H. MacDonald, N. P. Ong, Anomalous Hall effect. *Rev. Mod. Phys.* **82**, 1539–1592 (2010).

50. D. Xiao, M.-C. Chang, Q. Niu, Berry phase effects on electronic properties. *Rev. Mod. Phys.* **82**, 1959–2007 (2010).

51. H. Tsai, T. Higo, K. Kondou, T. Nomoto, A. Sakai, A. Kobayashi, T. Nakano, K. Yakushiji, R. Arita, S. Miwa, Y. Otani, S. Nakatsuji, Electrical manipulation of a topological antiferromagnetic state. *Nature* **580**, 608–613 (2020).

52. Y. Takeuchi, Y. Yamane, J. Y. Yoon, R. Itoh, B. Jinnai, S. Kanai, J. Ieda, S. Fukami, H. Ohno, Chiral-spin rotation of non-collinear antiferromagnet by spin-orbit torque. *Nat. Mater.* **20**, 1364–1370 (2021).

53. B. Pal, B. K. Hazra, B. Göbel, J.-C. Jeon, A. K. Pandeya, A. Chakraborty, O. Busch, A. K. Srivastava, H. Deniz, J. M. Taylor, H. Meyerheim, I. Mertig, S.-H. Yang, S. S. P. Parkin, Setting of the magnetic structure of chiral kagome antiferromagnets by a seeded spin-orbit torque. *Sci. Adv.* **8**, eabo5930 (2022).

54. A. K. Nayak, J. E. Fischer, Y. Sun, B. Yan, J. Karel, A. C. Komarek, C. Shekhar, N. Kumar, W. Schnelle, J. Kübler, C. Felser, S. S. P. Parkin, Large anomalous Hall effect driven by a nonvanishing Berry curvature in the noncolinear antiferromagnet Mn_3Ge. *Sci. Adv.* **2**, e1501870 (2016).

55. J. Železný, Y. Zhang, C. Felser, B. Yan, Spin-polarized current in noncollinear antiferromagnets. *Phys. Rev. Lett.* **119**, 187204 (2017).

56. L. Liu, O. J. Lee, T. J. Gudmundsen, D. C. Ralph, R. A. Buhrman, Current-induced switching of perpendicularly magnetized magnetic layers using spin torque from the spin Hall effect. *Phys. Rev. Lett.* **109**, 096602 (2012).

57. W. Kohn, L. J. Sham, Self-consistent equations including exchange and correlation effects. *Phys. Rev.* **140**, A1133-A1138 (1965).

58. G. Kresse, J. Furthmüller, Efficient iterative schemes forab initiototal-energy calculations using a plane-wave basis set. *Phys. Rev. B* **54**, 11169–11186 (1996).

59. J. P. Perdew, K. Burke, M. Ernzerhof, Generalized gradient approximation made simple. *Phys. Rev. Lett.* **77**, 3865–3868 (1996).

60. J. P. Perdew, J. A. Chevary, S. H. Vosko, K. A. Jackson, M. R. Pederson, D. J. Singh, C. Fiolhais, Atoms, molecules, solids, and surfaces: Applications of the generalized gradient approximation for exchange and correlation. *Phys. Rev. B* **46**, 6671–6687 (1992).

61. H. J. Monkhorst, J. D. Pack, Special points for Brillouin-zone integrations. *Phys. Rev. B* **13**, 5188–5192 (1976).

62. K. Koepernik, H. Eschrig, Full-potential nonorthogonal local-orbital minimum-basis band-structure scheme. *Phys. Rev. B* **59**, 1743–1757 (1999).

63. R. F. L. Evans, W. J. Fan, P. Chureemart, T. A. Ostler, M. O. A. Ellis, R. W. Chantrell, Atomistic spin model simulations of magnetic nanomaterials. *J. Phys. Condens. Matter* **26**, 103202 (2014).

64. F. J. dos Santos, N. Biniskos, S. Raymond, K. Schmalzl, M. dos Santos Dias, P. Steffens, J. Persson, S. Blügel, S. Lounis, T. Brückel, Spin waves in the collinear antiferromagnetic phase $_{of}Mn_5Si_3$. *Phys. Rev. B* **103**, 024407 (2021).

65. N. Biniskos, F. J. dos Santos, K. Schmalzl, S. Raymond, M. dos Santos Dias, J. Persson, N. Marzari, S. Blügel, S. Lounis, T. Brückel, Complex magnetic structure and spin waves of the noncollinear antiferromagnet Mn_5Si_3. *Phys. Rev. B* **105**, 104404 (2022).

66. R. F. L. Evans, U. Atxitia, R. W. Chantrell, Quantitative simulation of temperature-dependent magnetization dynamics and equilibrium properties of elemental ferromagnets. *Phys. Rev. B* **91**, 144425 (2015).

67. H. Sato, M. Yamanouchi, K. Miura, S. Ikeda, H. D. Gan, K. Mizunuma, R. Koizumi, F. Matsukura, H. Ohno, Junction size effect on switching current and thermal stability in CoFeB/MgO perpendicular magnetic tunnel junctions. *Appl. Phys. Lett.* **99**, 042501 (2011).

68. H. Sato, E. C. I. Enobio, M. Yamanouchi, S. Ikeda, S. Fukami, S. Kanai, F. Matsukura, H. Ohno, Properties of magnetic tunnel junctions with a MgO/CoFeB/Ta/CoFeB/MgO recording structure down to junction diameter of 11 nm. *Appl. Phys. Lett.* **105**, 062403 (2014).

69. W. Wernsdorfer, B. Doudin, D. Mailly, K. Hasselbach, A. Benoit, J. Meier, J. P. Ansermet, B. Barbara, Nucleation of magnetization reversal in individual nanosized nickel wires. *Phys. Rev. Lett.* **77**, 1873–1876 (1996).

70. F. Cayssol, D. Ravelosona, C. Chappert, J. Ferré, J. P. Jamet, Domain wall creep in magnetic wires. *Phys. Rev. Lett.* **92**, 107202 (2004).

71. H. Bai, W. Zhu, Y. You, X. Chen, X. Zhou, F. Pan, C. Song, Size-dependent anomalous Hall effect in noncollinear antiferromagnetic Mn_3Sn films. *Appl. Phys. Lett.* **117**, 052404 (2020).

72. Y. Sato, Y. Takeuchi, Y. Yamane, J.-Y. Yoon, S. Kanai, J. I. Ieda, H. Ohno, S. Fukami, Thermal stability of non-collinear antiferromagnetic Mn_3Sn nanodot. *Appl. Phys. Lett.* **122**, 122404 (2023).

73. S. Dong, H. Xiang, E. Dagotto, Magnetoelectricity in multiferroics: A theoretical perspective. *Natl. Sci. Rev.* **6**, 629–641 (2019).

74. X. He, N. Helbig, M. J. Verstraete, E. Bousquet, TB2J: A python package for computing magnetic interaction parameters. *Comput. Phys. Commun.* **264**, 107938 (2021).

75. A. I. Liechtenstein, M. I. Katsnelson, V. P. Antropov, V. A. Gubanov, Local spin density functional approach to the theory of exchange interactions in ferromagnetic metals and alloys. *J. Magn. Magn. Mater.* **67**, 65–74 (1987).